Acta Astronautica 123 (2016) 364–375

Contents lists available at ScienceDirect

Acta Astronautica

journal homepage: www.elsevier.com/locate/actaastro

Invited Paper

Bounded relative orbits about asteroids for formation flying and applications

Nicola Baresi *, Daniel J. Scheeres *, Hanspeter Schaub *

Department of Aerospace Engineering Sciences, University of Colorado Boulder, 80309 Boulder, CO, United States

ARTICLE INFO

Article history:
Received 21 July 2015
Received in revised form
10 December 2015
Accepted 23 December 2015
Available online 4 January 2016

Keywords:
Formation flying
Asteroids
Lagrange Planetary Equations
Dynamical system theory
Quasi-periodic invariant tori

ABSTRACT

The relative motion about 4179 Toutatis is studied in order to investigate the feasibility of formation flying as an alternative concept for future asteroid exploration missions. In particular, the existence of quasi-frozen orbits about slowly rotating bodies allows us to compute families of periodic orbits in the body-fixed frame of the asteroid. Since these periodic orbits are of the *center* × *center* type, quasi-periodic invariant tori are calculated via fully numerical procedures and used to initialize spacecraft formations about the central body. Numerical simulations show that the resulting in-plane and out-of-plane relative trajectories remain bounded over long time spans; i.e., more than 30 days.

1. Introduction

In this thriving era for small bodies exploration, it may be interesting to study the relative motion of satellites flying in a formation about asteroids or comets. Such a concept is not novel and has already been proposed as a potential benefit for several asteroid mitigation strategies. For instance, Maddock and Vasile considered formations of solar concentrators to deflect hazardous Near Earth Asteroids (NEA) by surface ablation [1]. Alternatively, Gong et al. proved the reliability of solar-sail formations in displaced orbits as effective and powerful gravity tractors [2].

A common denominator in the literature, however, is that the gravitational attraction of the asteroid is usually neglected or oversimplified. Both Gong [2] and Vasile [3] approximate the gravitational pull excerted by the central body via a point-mass gravity field. Only recently, Foster et al. considered multiple gravity tractors in a high-order spherical harmonics gravity field, but instead of designing cost-free relative trajectories, the authors were focused on controlling the satellites at fixed locations with respect to the Sun-asteroid rotating frame to maximize the effects of their proposed deflection strategy [4]. Accordingly, passive relative orbits in the proximity of small bodies are yet to be found and described.

In this paper, a systematic approach to establish bounded relative motion about slowly rotating tri-axial ellipsoids is presented. As a case study, a chief and a deputy spacecraft are considered while flying in a formation about 4179 Toutatis, a slowly rotating asteroid that was flown-by China's Chang'e 2 spacecraft in December 2012 [5]. Because of the existence of quasi-frozen orbits in the body-fixed frame of the asteroid [6], the secular evolution of the mean orbit elements of the satellites can be studied via Lagrange Planetary Equations [7]. Moreover, first-order bounded relative motion conditions can be derived by matching the averaged drift rates due to the nonspherical shape of the central body [8]. As these bounded relative motion conditions are based on mean orbit element differences, the applicability of using a first-order mean-to-osculating orbit element mapping for spacecraft formations about Toutatis is also investigated and used to motivate additional numerical analyses. Specifically, stable periodic orbits are computed starting

* Corresponding authors.
E-mail addresses: nicola.baresi@colorado.edu (N. Baresi), scheeres@colorado.edu (D.J. Scheeres), hanspeter.schaub@colorado.edu (H. Schaub).

http://dx.doi.org/10.1016/j.actaastro.2015.12.033
0094-5765/

from the output of the mean-to-osculating orbit element mapping and using a Poincaré map between consecutive surface of section crossings [9]. Then, Kolemen's method is applied to extend the center submanifolds beyond the linear regime, and to compute quasi-periodic orbits that foliate two dimensional invariant tori in the neighborhood of the original periodic orbit [10]. Finally, the relative motion between satellites initialized on the quasi-periodic tori as well as on the computed periodic orbit is studied. In particular, numerical simulations investigate the long-term behavior of the relative motion and assess the robustness of the derived initial conditions while taking into account unmodeled forces such as solar radiation pressure and third body attraction.

2. Bounded relative orbit conditions

According to Reference [9], the majority of the perturbations felt by mass particles about asteroids are due to the second degree and order gravity field. Thus, for preliminary Formation Flying mission analyses, it is possible to consider the gravitational potential as given by

$$U=\frac{\mu}{r}+R=\frac{\mu}{r}\left\{1+\left(\frac{r_0}{r}\right)^2\left[C_{20}\left(\frac{3}{2}\sin^2\delta-\frac{1}{2}\right)-3C_{22}\cos(2\lambda)\left(\sin^2\delta-1\right)\right]\right\}, \tag{1}$$

where μ is the gravitational parameter of the central body, r is the distance of the satellite from the center of the asteroid, δ and λ are its latitude and longitude with respect to the first principal axis, respectively, r_0 is the scale factor, and $C_{20}=-J_2$ and C_{22} are respectively the second zonal and second-degree second-order spherical harmonics coefficients.

Assuming that the asteroid is rotating about its maximum axis of inertia, one can rewrite δ and λ via

$$\sin\delta=\sin i\sin u, \tag{2a}$$

$$\tan\lambda=\frac{\sin\Omega_R\cos u+\cos\Omega_R\sin u\cos i}{\cos\Omega_R\cos u-\sin\Omega_R\sin u\cos i}, \tag{2b}$$

where i is the inclination of the spacecraft, $u=\omega+f$ is the argument of latitude, $\Omega_R=\Omega-\omega_T t$ is the longitude of the ascending node with respect to the rotating body-fixed frame of the asteroid, and ω_T is the spin rate of the central body. Furthermore, if the mean motion of the spacecraft is much larger than ω_T, all of the orbit elements can be regarded as constant over one orbit period [6]. Then, it is also possible to consider the averaged perturbing function over the mean anomaly M, i.e.,

$$\overline{R}=\frac{1}{2\pi}\int_0^{2\pi}R\,\mathrm{d}M=\frac{\mu r_0^2}{2a^3(1-e^2)^{3/2}}\left[C_{20}\left(\frac{3}{2}\sin^2 i-1\right)-3C_{22}\sin^2 i\cos(2\Omega_R)\right] \tag{3}$$

and investigate the evolution of the spacecraft mean orbit elements with Lagrange Planetary Equations [7].

It turns out that for a very slow rotator such as 4179 Toutatis ($P_T=2\pi/\omega_T\simeq 5.43$ days), the mean orbital element rates can be rewritten as [6,8]

$$a'=0, \tag{4a}$$

$$e'=0, \tag{4b}$$

$$i'=\frac{3C_{22}\sin i\sin(2\Omega_R)}{\eta^4L^7}, \tag{4c}$$

$$\Omega_R'=\frac{3\cos i(C_{20}+2C_{22}\cos(2\Omega_R))}{2\eta^4L^7}-\frac{\omega_T}{n_0}, \tag{4d}$$

$$\omega'=-\frac{15\cos(2i)(C_{20}+2C_{22}\cos(2\Omega_R))+9C_{20}-6C_{22}\cos(2\Omega_R)}{8\eta^4L^7}, \tag{4e}$$

$$M'=\frac{1}{L^3}+\frac{9\sin^2 i(C_{20}+2C_{22}\cos(2\Omega_R))-6C_{20}}{4\eta^3L^7}, \tag{4f}$$

where

$$(\cdot)'=\frac{1}{n_0}\frac{\mathrm{d}}{\mathrm{d}t}, \tag{5a}$$

$$n_0=\sqrt{\mu/r_0^3}, \tag{5b}$$

$$\eta=\sqrt{1-e^2}, \tag{5c}$$

$$L=\sqrt{a/r_0}. \tag{5d}$$

Accordingly, the semi-major axis and the eccentricity are constant on average, whereas the inclination, body-fixed longitude of ascending node, argument of periapse, and mean anomaly have secular variations that depend on a, e, i, and Ω_R.

It is worth noting that the latter may become an issue for the design of bounded relative trajectories about strongly elongated bodies. In fact, in order to establish bounded relative motion, one should carefully choose the values of a, e, i, and Ω_R, and try to minimize the difference between the mean orbit element rates of the spacecraft within the formation [8]. However, for any specified value of i and Ω_R, the mean inclination and the mean body-fixed longitude of the ascending node will be changing according to (4c) and (4d) unless i' and Ω_R' are somehow nullified.

As suggested by Hu and Scheeres [6], this is actually possible for orbiters about slowly rotating bodies that satisfy $|w_T/B|<1$, where $B=(3n/2p^2)[2C_{22}-C_{20}]r_0^2$. Then,

$$\Omega_R=\pm\pi/2, \tag{6a}$$

$$\cos i=-\omega_T/B \tag{6b}$$

nullify (4c) and (4d). The relationships (6) are known as the quasi-frozen orbit conditions and can be used in combination with (4) to infer second-order second-degree bounded relative motion conditions.

To that end, consider a formation of two satellites where a, e, i, Ω_R, ω, and M will be referred to as the mean orbit elements of the chief, whereas a_d, e_d, i_d, $\Omega_{R,d}$, ω_d, and M_d will be used to indicate the mean orbit elements of the deputy spacecraft. We will also refer to $\delta i'$, $\delta\Omega_R'$, $\delta\omega'$, and $\delta M'$ as the first variations of $i_d'-i'$, $\Omega_{R,d}'-\Omega_R'$, $\omega_d'-\omega'$, and $M_d'-M'$ respectively.

It can immediately be noted that $\delta i'$, $\delta\Omega_R'$, $\delta\omega'$, and $\delta M'$ would vanish if $L_d = L$, $\eta_d = \eta$, $i_d = i$, and $\Omega_{R,d} = \Omega_R$ (in-plane formations). Such a selection would guarantee bounded relative motion but would also leave less freedom in the design of the relative trajectory. The same happens whenever the chief and the deputy are initialized with the same set of mean orbit elements, except for the mean anomaly at epoch, i.e., $M_d \neq M$ (Leader–Follower formations). Alternatively, following the derivation of the J_2-invariant relationships [8], one could look at the first variation of the mean argument of latitude, i.e., $\theta_M = M + \omega$, and try to nullify $\delta\theta_M' = \delta M' + \delta\omega'$ instead of $\delta\omega'$ and $\delta M'$. Then, the more general second-order second-degree bounded relative orbit relationships will be given by

$$\delta i' = \frac{\partial i'}{\partial L}\delta L + \frac{\partial i'}{\partial \eta}\delta\eta + \frac{\partial i'}{\partial i}\delta i + \frac{\partial i'}{\partial \Omega_R}\delta\Omega_R = 0, \tag{7a}$$

$$\delta\Omega_R' = \frac{\partial \Omega_R'}{\partial L}\delta L + \frac{\partial \Omega_R'}{\partial \eta}\delta\eta + \frac{\partial \Omega_R'}{\partial i}\delta i + \frac{\partial \Omega_R'}{\partial \Omega_R}\delta\Omega_R = 0, \tag{7b}$$

$$\delta\theta_M' = \frac{\partial \theta_M'}{\partial L}\delta L + \frac{\partial \theta_M'}{\partial \eta}\delta\eta + \frac{\partial \theta_M'}{\partial i}\delta i + \frac{\partial \theta_M'}{\partial \Omega_R}\delta\Omega_R = 0. \tag{7c}$$

From Eqs. (7a) and (7b), it follows that

$$C_{22}\sin(2\Omega_R)[\eta\cos i\delta i - \sin i(4L\delta\eta + 7\eta\delta L)] + 2C_{22}\eta L\sin i\cos(2\Omega_R)\delta\Omega_R = 0, \tag{8a}$$

$$[C_{20} + 2C_{22}\cos(2\Omega_R)][\cos i(4L\delta\eta + 7\eta\delta L) + \delta i\eta L\sin i] + 4C_{22}\eta L\cos i\sin(2\Omega_R)\delta\Omega_R = 0, \tag{8b}$$

which, when evaluated at the quasi-frozen orbit conditions (6a)–(6b), simplify in

$$-\frac{2}{B}C_{22}\omega_T\eta L\Gamma\delta\Omega_R = 0, \tag{9a}$$

$$-7\eta\delta L - 4L\delta\eta + \eta L\Gamma\delta i = 0, \tag{9b}$$

with

$$\Gamma = \sqrt{(B/\omega_T)^2 - 1}. \tag{10}$$

Consequently, in order to satisfy the bounded relative orbit conditions (7a) and (7c), $\delta\Omega_R$ must always be equal to zero, i.e., $\Omega_{R,d} = \Omega_R$. Furthermore, substituting Eq. (9a) and (9b) into Eq. (7c) yields

$$\delta i = \frac{B^2\left(7C_{20} - 42C_{22} + 16\eta^3L^4\right) - 21\omega_T^2(C_{20} - 2C_{22})}{B^2\left[7(\eta+1)(C_{20} - 6C_{22}) + 4\eta^4L^4\right] + 7\omega_T^2(3\eta+5)(C_{20} - 2C_{22})}\frac{1}{\Gamma}\delta\eta, \tag{11}$$

which can also be substituted back into Eq. (9b) to get the final set of first-order mean orbit element relationships as a function of $\delta\eta$:

$$\delta L = -\frac{(3\eta+4)L\left[B^2(C_{20} - 6C_{22}) + 5\omega_T^2(C_{20} - 2C_{22})\right]}{B^2\left[7(\eta+1)(C_{20} - 6C_{22}) + 4\eta^4L^4\right] + 7\omega_T^2(3\eta+5)(C_{20} - 2C_{22})}\frac{1}{\eta}\delta\eta. \tag{12}$$

Thus, for small values of $\delta\eta = \eta_d - \eta$, Eqs. (11) and (12) give the mean inclination and semi-major axis differences that minimize the secular drift induced by second-order second-degree gravity terms. Also notice that for $C_{22} = 0$, $\omega_T = -B\cos i$, Eqs. (11) and (12) reduce to the J_2-invariant orbit relationships derived in Reference [8].

3. Mean/osculating orbit element mapping

The second-order second-degree bounded relative orbit conditions have been derived in the mean orbit element space. Thus, it is necessary to implement a reliable mean-to-osculating orbit element mapping in order to design spacecraft formation about slowly rotating asteroids. To that end, a first-order Lie–Deprit transformation is implemented to convert from mean to osculating orbit elements and vice versa [11]. The generating functions used for the conversion can be found in De Saedeleer and Henrard [12].

Fig. 1 shows a comparison between two different chief trajectories integrated in the rotating body-fixed frame of the asteroid for four weeks, i.e., more than 70 Orbital Periods (OP), with a second-order second-degree gravity field [9]. Both the trajectories are initialized on a quasi-frozen orbit with Keplerian orbit elements given by

$$æ_c = [a \quad e \quad i \quad \Omega \quad \omega \quad M]^T,$$

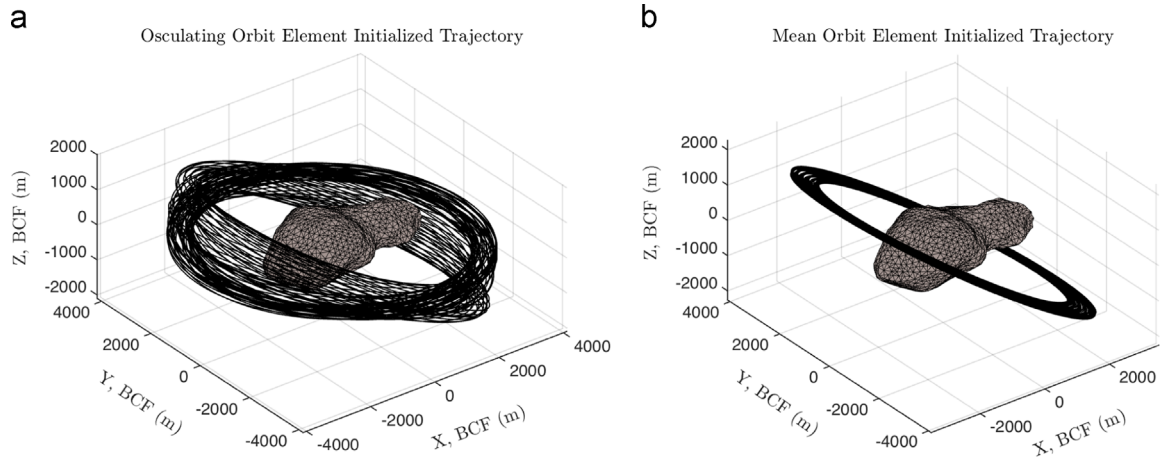

Fig. 1. Chief body-fixed trajectory set up in osculating orbit elements (a) and mean orbit elements (b).

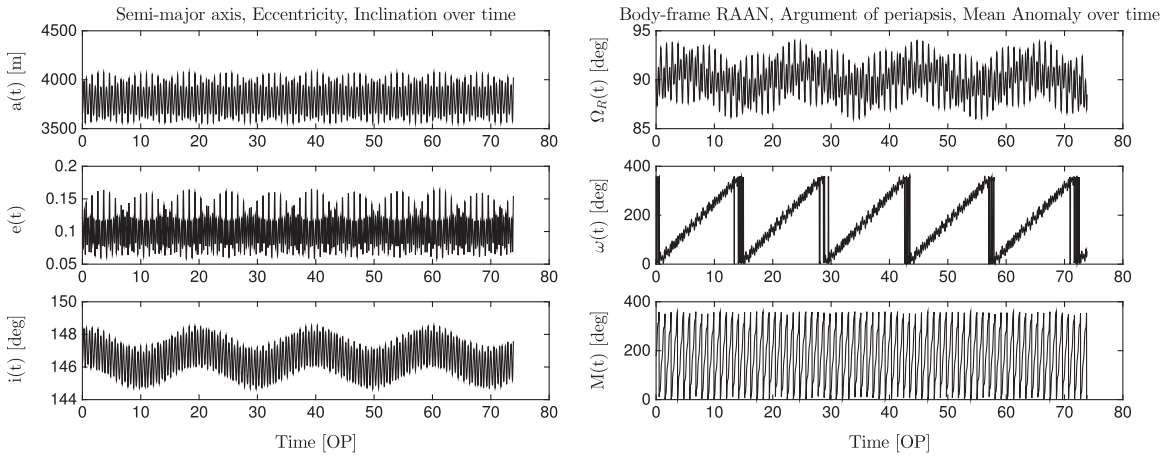

Fig. 2. Osculating orbit elements for the mean orbit element initialized trajectory.

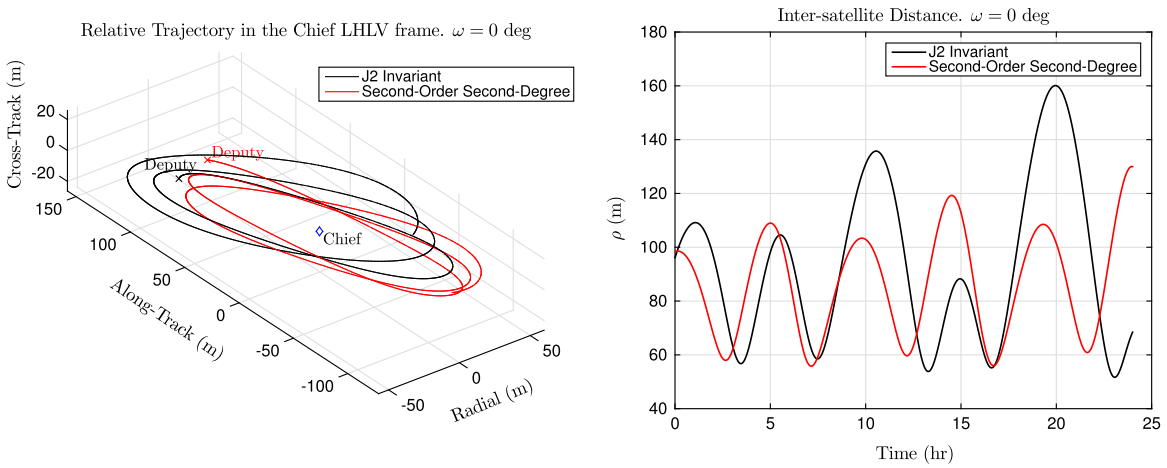

Fig. 3. J_2-invariant and second-order second-degree out-of-plane relative trajectories with $\delta i = 0.4°$, $\delta\omega = 8°$, $\delta M = -8°$, and $\omega = 0°$.

$$= [3800 \quad 0.10 \quad 147.22 \quad 90.00 \quad 0.00 \quad 180.00]^T \quad (\mathrm{m}, -, \mathrm{deg}). \tag{13}$$

However, in the plot of Fig. 1(b) the initial conditions (13) are first converted with the aforementioned Lie–Deprit transformation.

As expected, the trajectory initialized via mean orbit elements (Fig. 1(b)) displays a much nicer behavior than the one initialized using osculating orbit elements (Fig. 1(a)). However, even for the mean orbit element case, the time histories of the chief osculating orbit elements shown in Fig. 2 reveal that second-order effects can hardly be neglected for orbiters about Toutatis ($C_{20} \simeq -0.31$, $C_{22} \simeq 0.12$). In fact, the first-order Lie–Deprit transformation fails to yield initial conditions for which the inclination and the body-fixed RAAN are truly constant on average.

In addition to that, approximations in the transformation are even more evident when looking at different relative trajectories generated with the same mean-to-osculating orbit element mapping. That is, even though the obtained relative trajectories are more performant than the standard J_2 invariant orbits (Figs. 3 and 4), it appears as the initial conditions of the chief highly affect the long-term behavior of the relative orbit. For instance, Fig. 5(a) shows the in-plane relative trajectory of the deputy with $\delta\omega = -\delta M = 8°$ when the mean orbit elements of the chief are set equal to (13). As it can be seen, the relative trajectory looks much more stable than the one obtained when ω is changed to 90° (Fig. 5b). Since such variable only appears in the mean-to-osculating orbit element mapping, it seems as the first-order Lie–Deprit transformation currently available in the literature is not accurate enough to design long-term bounded relative trajectories about strongly elongated bodies.

For this reason, consider switching to a fully numerical approach that involves the numerical computation of periodic and quasi-periodic orbits about Toutatis. After all, the approximate Lie–Deprit transformation indeed succeeds in generating trajectories that are close to be periodic (Fig. 1(b)). Therefore, starting from the output of the mean-to-osculating orbit element mapping, one can try to further refine the initial conditions and compute families of periodic orbits about the target asteroid [13]. If the computed periodic orbits have a center component, then

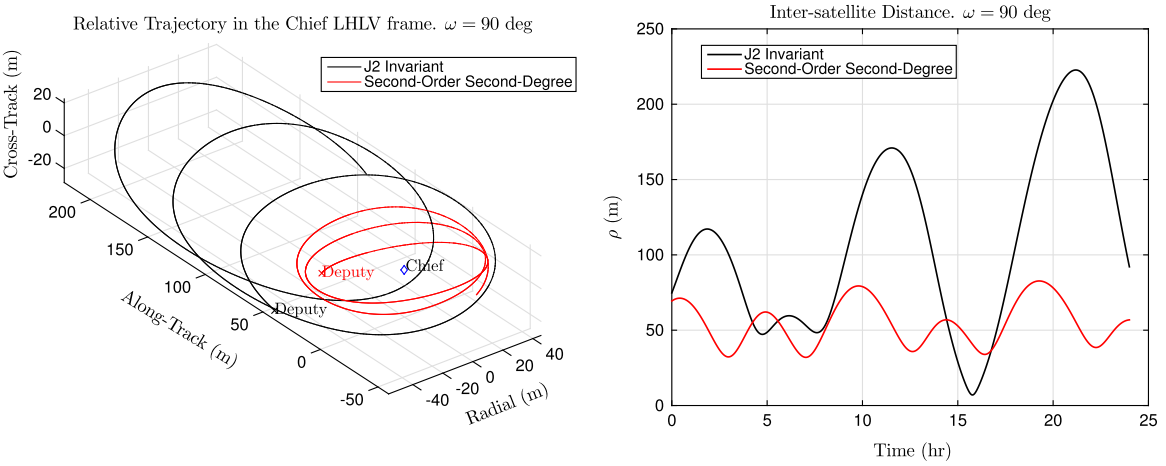

Fig. 4. J_2-invariant and second-order second-degree out-of-plane relative trajectories with $\delta i = 0.4°$, $\delta\omega = 8°$, $\delta M = -8°$, and $\omega = 90°$.

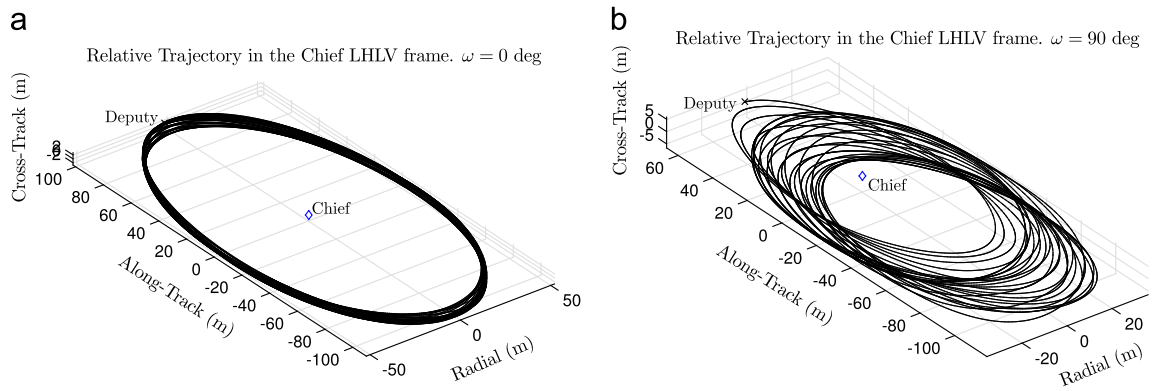

Fig. 5. In-plane relative trajectories with $\delta\omega = -\delta M = 8°$ for the case $\omega = 0°$ (a) and $\omega = 90°$ (b).

quasi-periodic invariant tori can be used to initialize spacecraft formations that are guaranteed to remain bounded over long time spans. Such a strategy was first suggested by Barden and Howell [14], and it will be hereby applied for the first time to design bounded relative trajectories about small bodies.

4. Equations of motion

In order to compute periodic and quasi-periodic orbits, consider the equations of motion for one spacecraft in orbit about 4179 Toutatis. The asteroid is modeled as a tri-axial ellipsoid with semi-major axes $\alpha = 2250$ m, $\beta = 1200$ m, and $\gamma = 950$ m and constant density $\sigma = 2500$ kg/m^3 (Fig. 6). Moreover, although Toutatis is a non-principal axis rotator [15], it is assumed that the angular velocity vector of the body is aligned with the third axis $\hat{e}_3$ of an inertial reference frame $\mathcal{N} = \{\mathcal{O}, \hat{e}_1, \hat{e}_2, \hat{e}_3\}$ centered on the body and oriented such that $\hat{e}_1$, $\hat{e}_2$, and $\hat{e}_3$ are parallel to the asteroid principal axes of inertia at time $t_0 = 0$. That is, $\boldsymbol{\omega} = \omega_T\, \hat{e}_3$, where $\omega_T = 1.34 \times 10^{-5}$ rad/s. This assumption enables the analytical results of Ref. [6], which provide good initial guesses for the numerical computation of periodic orbits in the vicinity of the target asteroid (Fig. 1(b)).

To that end, consider a second rotating reference frame such that $\hat{b}_1$, $\hat{b}_2$, and $\hat{b}_3$ are always aligned with the asteroid principal axes of inertia. Thus, let $\mathcal{B} = \{\mathcal{O}, \hat{b}_1, \hat{b}_2, \hat{b}_3\}$ be denoted as the Body-Centered-Body-Fixed frame (BCF) and $\mathcal{N} = \{\mathcal{O}, \hat{b}_1, \hat{b}_2, \hat{b}_3\}$ as the Body-Centered-Inertial frame (BCI).

In BCF, the equations of motion of a single satellite are given by [16]

$$\begin{cases} \ddot{x} &= \omega_T^2 x + 2\omega_T \dot{y} + U_x, \\ \ddot{y} &= \omega_T^2 y - 2\omega_T \dot{x} + U_y, \\ \ddot{z} &= U_z, \end{cases} \tag{14}$$

where $\boldsymbol{X} = [x\ y\ z\ \dot{x}\ \dot{y}\ \dot{z}]^T$ is the state of the spacecraft in the rotating frame, and

$$U_x = \frac{\partial U}{\partial x} = -\frac{3}{2}\mu x \int_0^\infty \left(\frac{1}{\alpha^2 + \Lambda + \nu}\right) \frac{d\nu}{\Delta(\nu + \Lambda)}, \tag{15a}$$

$$U_y = \frac{\partial U}{\partial y} = -\frac{3}{2}\mu y \int_0^\infty \left(\frac{1}{\beta^2 + \Lambda + \nu}\right) \frac{d\nu}{\Delta(\nu + \Lambda)}, \tag{15b}$$

$$U_z = \frac{\partial U}{\partial z} = -\frac{3}{2}\mu z \int_0^\infty \left(\frac{1}{\gamma^2 + \Lambda + \nu}\right) \frac{d\nu}{\Delta(\nu + \Lambda)}, \tag{15c}$$

are the partial derivatives of the potential

$$U = -\mu\frac{3}{4}\int_0^\infty \phi(x,y,z,\nu+\Lambda)\frac{d\nu}{\Delta(\nu+\Lambda)}, \tag{16}$$

with

$$\Delta(\nu+\Lambda) = \sqrt{(\alpha^2+\Lambda+\nu)(\beta^2+\Lambda+\nu)(\gamma^2+\Lambda+\nu)}, \tag{17a}$$

$$\phi(x,y,z,\nu+\Lambda) = \frac{x^2}{\alpha^2+\Lambda+\nu}+\frac{y^2}{\beta^2+\Lambda+\nu}+\frac{z^2}{\gamma^2+\Lambda+\nu}-1. \tag{17b}$$

Observe that U depends on both the gravitational parameter of the body, i.e.,

$$\mu = 1792.60\ \mathrm{m}^3/\mathrm{s}^2, \tag{18}$$

and Λ, which is defined to be either the positive root of $\phi(x,y,z,\Lambda)=0$ whenever U is computed outside of the ellipsoid, or zero otherwise. Then, both (15) and (16) can be evaluated via the Carlson elliptic integrals described in Ref. [17].

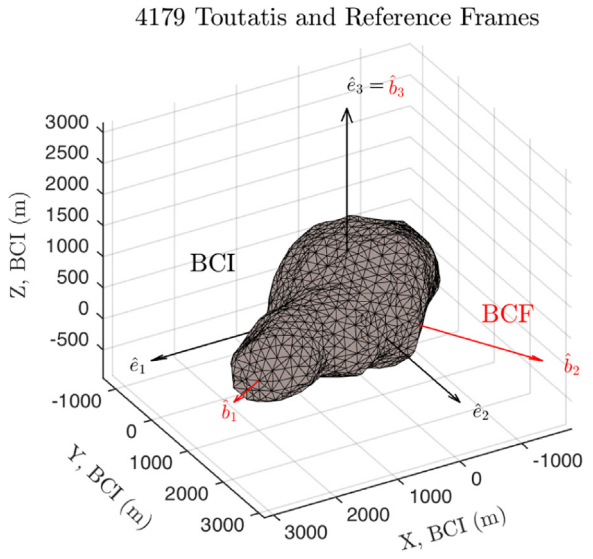

Fig. 6. Asteroid 4179 Toutatis and reference frames.

It is also worth noting that the system (14) admits an integral of motion given by

$$C = -\tfrac{1}{2}\left(\dot{x}^2+\dot{y}^2+\dot{z}^2\right)+\tfrac{1}{2}\omega_T^2(x^2+y^2)+U, \tag{19}$$

and known as the Jacobi constant. Moreover, the equations of motion (14) can be easily linearized via

$$\dot{\boldsymbol{X}} = A\boldsymbol{X} \tag{20}$$

where

$$\begin{bmatrix} A=0 & 0 & 0 & 1 & 0 & 0 \\ 0 & 0 & 0 & 0 & 1 & 0 \\ 0 & 0 & 0 & 0 & 0 & 1 \\ \omega_T^2+U_{xx} & U_{xy} & U_{xz} & 0 & 2\omega_T & 0 \\ U_{xy} & \omega_T^2+U_{yy} & U_{yz} & -2\omega_T & 0 & 0 \\ U_{xz} & U_{yz} & U_{zz} & 0 & 0 & 0, \end{bmatrix} \tag{21}$$

and U_{xx}, U_{xy}, U_{xz}, U_{yy}, U_{yz}, and U_{zz} are the second partial derivatives of the potential (16) (see Ref. [9] for details). Accordingly, the State Transition Matrix $\Phi(t,t_0)$ can be integrated along with Eq. (14) via

$$\dot{\Phi}(t,t_0) = A\Phi(t,t_0), \quad \Phi(t_0,t_0) = I_{6\times6}, \tag{22}$$

where $I_{6\times6}$ is the 6×6 identity matrix.

5. Periodic orbits about 4179 Toutatis

Integrating the initial conditions provided by the Lie–Deprit transformation with Eq. (14) yields the trajectory portrayed in Fig. 7(a). As it can be seen, the satellite is very close to be on a periodic trajectory, so that numerical procedures can be implemented in order to refine the initial conditions and achieve periodic motion.

Notice that the spacecraft pierces the x–y plane twice along its orbit: one with $\dot{z}>0$, and one with $\dot{z}<0$. Accordingly, $S(\boldsymbol{x}) = z$, $\dot{z}<0$ is a valid surface of section that can be used to compute a linearized Poincaré Map and its associated monodromy matrix.

Given the reduced state $\boldsymbol{y} = [x\ y\ \dot{x}\ \dot{y}]^T$, it turns out that deviations on the surface of section at time t_0, namely $\delta\boldsymbol{y}_0$,

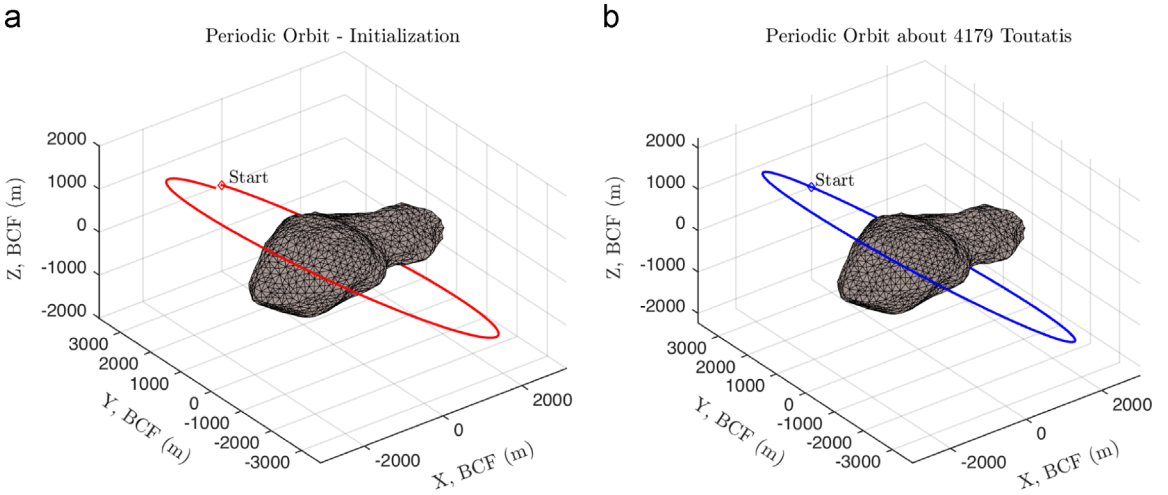

Fig. 7. Initial guess and final periodic orbit in the BCF frame.

can be mapped into deviations at the next surface of section crossing via [9]

$$\delta \boldsymbol{y}_1 = \Phi_{10}\delta \boldsymbol{y}_0, = P_0^T P_S \Phi(t_1,t_0)(P_0+P_H)\delta \boldsymbol{y}_0 \tag{23}$$

where

$$P_0 = \begin{bmatrix} I_{2\times 2} & 0_{2\times 2} \\ 0_{1\times 2} & 0_{1\times 2} \\ 0_{2\times 2} & I_{2\times 2} \\ 0_{1\times 2} & 0_{1\times 2} \end{bmatrix}, \quad P_S = [I_{6\times 6}] - \frac{1}{\left.\frac{\partial S}{\partial \boldsymbol{x}}\right|_1 \cdot \dot{\boldsymbol{x}}(t_1)} \dot{\boldsymbol{x}}(t_1) \left.\frac{\partial S}{\partial \boldsymbol{x}}\right|_1, \tag{24}$$

$$P_H = \frac{1}{\dot{z}_0}\begin{bmatrix} 0 & 0 & 0 & 0 \\ 0 & 0 & 0 & 0 \\ 0 & 0 & 0 & 0 \\ 0 & 0 & 0 & 0 \\ 0 & 0 & 0 & 0 \\ (\omega_T^2 x_0 + U_{x_0}) & (\omega_T^2 y_0 + U_{y_0}) & -\dot{x}_0 & -\dot{y}_0 \end{bmatrix}. \tag{25}$$

Consequently, if $\boldsymbol{y}_1 = \boldsymbol{g}(\boldsymbol{y}_0, C)$ is the full nonlinear Poincaré Map from an initial point $\boldsymbol{y}_0$ and fixed energy C to the next surface of section crossing $\boldsymbol{y}_1$,

$$\begin{aligned} \boldsymbol{y}_0 + \delta \boldsymbol{y}_0 &= \boldsymbol{g}(\boldsymbol{y}_0 + \delta \boldsymbol{y}_0, C), = \boldsymbol{g}(\boldsymbol{y}_0, C) + \left[\frac{\partial \boldsymbol{g}}{\partial \boldsymbol{y}}\right]\delta \boldsymbol{y}_0 + \ldots \\ &= \boldsymbol{y}_1 + [\Phi_{10}]\delta \boldsymbol{y}_0 + \ldots \end{aligned} \tag{26}$$

and

$$\delta \boldsymbol{y}_0 = [I_{4\times 4} - \Phi_{10}]^{-1}(\boldsymbol{y}_1 - \boldsymbol{y}_0). \tag{27}$$

Eq. (27) can be used to update the initial guess $\boldsymbol{y}_0$ until a fixed point for the full nonlinear map is found. After five iteration, the algorithm converges to

$$\boldsymbol{y}_0 = \left[\, 1.3185 \times 10^{-11} \quad 3679.9296 \quad 0.5812 \quad 2.1991 \times 10^{-14} \,\right]^T (\mathrm{m, m/s}) \tag{28}$$

which corresponds to the periodic orbit illustrated in Fig. 7(b) ($C = 0.2145$, hence $\dot{z} = -0.4302$ m/s).

It is now possible to continue along the different members of the periodic orbit family by varying the value of the Jacobi integral as follows: given the periodic orbit of Fig. 7(b), $\boldsymbol{y}^* = \boldsymbol{g}(\boldsymbol{y}^*, C)$ implies

$$\boldsymbol{y}^* + \delta \boldsymbol{y} = \boldsymbol{g}(\boldsymbol{y}^* + \delta \boldsymbol{y}, C + \delta C), \simeq \boldsymbol{g}(\boldsymbol{y}^*, C) + \Phi_{10}\delta \boldsymbol{y} + \left[\frac{\partial \boldsymbol{g}}{\partial C}\right]\delta C,$$

i.e.,

$$\delta \boldsymbol{y} = [I_{4\times 4} - \Phi_{10}]^{-1}\left[\frac{\partial \boldsymbol{g}}{\partial C}\right]\delta C, \tag{29}$$

where

$$\left[\frac{\partial \boldsymbol{g}}{\partial C}\right] = P_0^T P_S \Phi(T,0)\begin{bmatrix} 0 & 0 & 0 & 0 & 0 & \frac{1}{C_{\dot{z}}} \end{bmatrix}^T, \tag{30a}$$

$$C_{\dot{z}} = \frac{\partial C}{\partial \dot{z}} = -\dot{z}. \tag{30b}$$

The new initial guess computed with (29) can now be used to initialize Eq. (27) and converge to a new periodic orbit at a different value of energy $C^* = C + \delta C$.

Fig. 8 displays a family of periodic orbits computed at different values of the Jacobi constant for either $\Omega_R = -90^\circ$ or $\Omega_R = 90^\circ$. As it can be seen, changing the value of C yields periodic orbits at different inclinations, thus giving the possibility to investigate the central body at different latitudes.

Also notice that the monodromy matrices $M = \Phi_{10}(T,0)$ computed along the periodic orbits typically admit two pairs of complex conjugate eigenvalues with unity magnitude. That is, Fig. 9 shows the root locus of M for the family of periodic orbits of Fig. 8(a). Except for a very few cases where the periodic orbit becomes unstable, the eigenvalues are usually distributed along the unit circle of the complex plane. In particular, for the periodic orbit of Fig. 7(b), the eigenvalues of the monodromy matrix are

$$\lambda_{12} = 0.9609 \pm \mathbf{I}\, 0.2770, \tag{31a}$$

$$\lambda_{34} = 0.9016 \pm \mathbf{I}\, 0.4326. \tag{31b}$$

Therefore, the periodic orbit turns out to be stable and surrounded by two families of quasi-periodic invariant tori (one for each pair of complex conjugate eigenvalues) [18].

By computing single members within the families, one can eventually come up with initial conditions for establishing long-term bounded relative motion about the

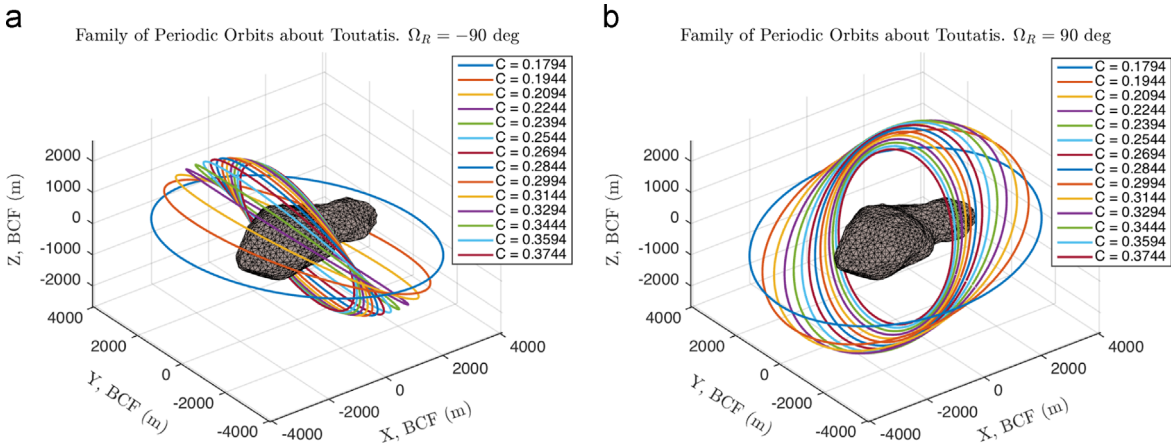

Fig. 8. Families of periodic orbits for $\Omega_R = -90^\circ$ and $\Omega_R = 90^\circ$.

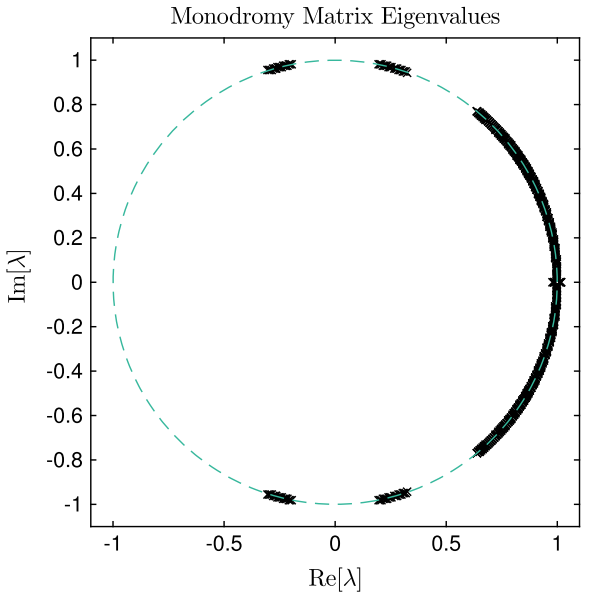

Fig. 9. Distribution of the Monodromy matrix eigenvalues for families of periodic orbits about 4179 Toutatis.

target asteroid. In fact, if multiple spacecraft are initialized on the surface of a quasi-periodic invariant torus, they would not only be guaranteed to remain on the surface, but they would also evolve around the central body with the same frequencies, thus without drifting apart from each other [14,19]. Accordingly, consider the numerical method outlined in the next section for computing quasi-periodic invariant tori about 4179 Toutatis.

6. Quasi-periodic orbits about Toutatis

Following the approach of Kolemen et al. [10], quasi-periodic tori can be computed as follows. First, notice that for a given eigenvalue/eigenvector pair, e.g., $\lambda = \lambda_{12}$, $\boldsymbol{v} = \boldsymbol{v}_{12} = \boldsymbol{v}_1 \pm \mathbf{i}\boldsymbol{v}_2$, it is possible to compute the invariant circle of the monodromy map M. That is, for any $\theta \in [0, 2\pi]$ and magnitude κ, we can define

$$\psi(\theta) = \kappa \cos \theta \boldsymbol{v}_1 - \kappa \sin \theta \boldsymbol{v}_2, \tag{32}$$

such that $M\psi(\theta) = \psi(\theta + \eta)$ (see Kolemen's paper for proof).

Although $\psi(\theta)$ should not be confused with the invariant set of the Poincaré section defined by the intersection between the quasi-periodic torus and $S(\boldsymbol{x})$, it is a linear

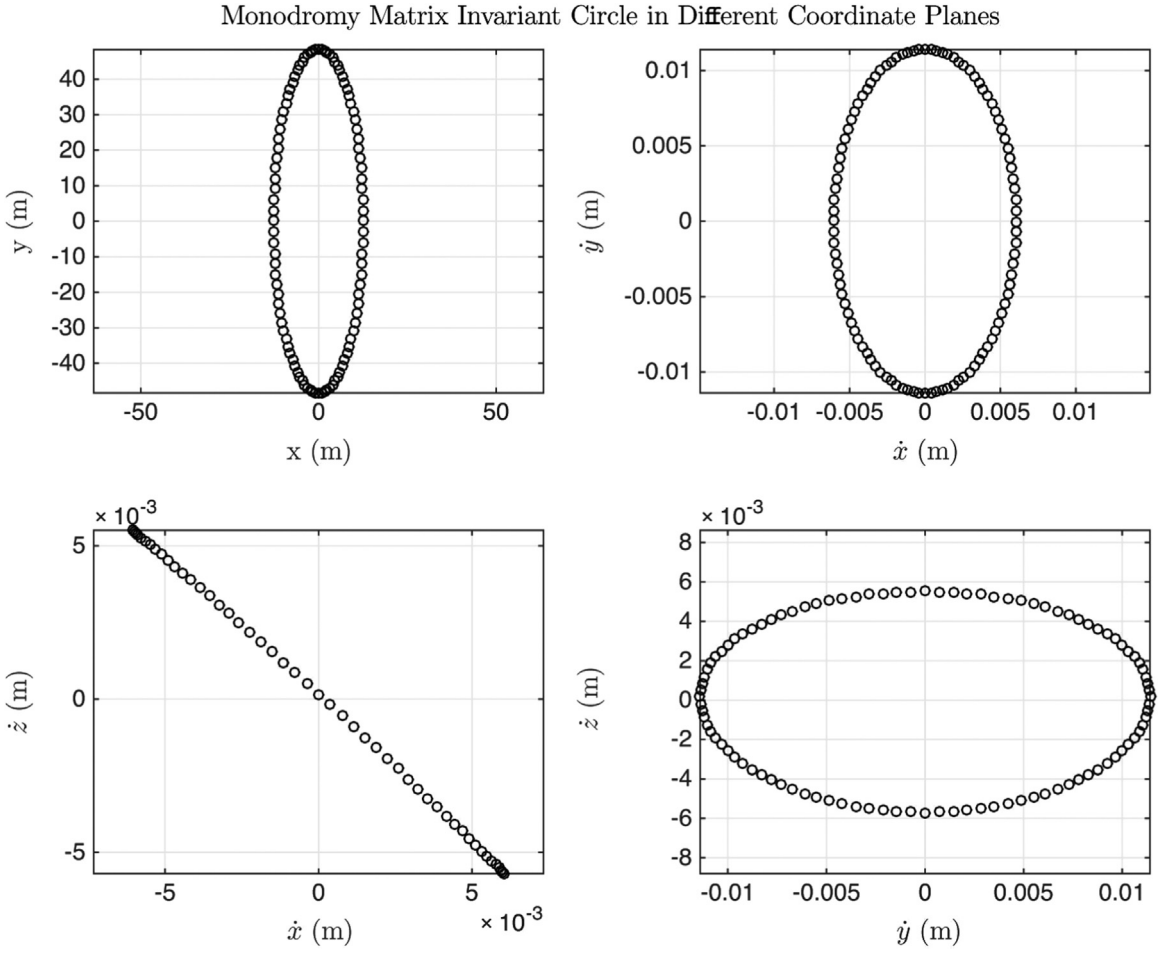

Fig. 10. Monodromy matrix invariant circle in different coordinate planes.

approximation of the relative distance between the torus and the periodic orbit under investigation. Therefore, it can be used to initialize a Newton iteration scheme aimed to compute the actual invariant set of the surface of section.

To that end, consider $N=100$ points on the invariant circle of the map M defined by $\boldsymbol{x}_{0,i}=\psi(\theta_i)$ with $\theta_i=2\pi(i-1)/N$, $i=1,\ldots,N$. Fig. 10 shows how the points $\boldsymbol{x}_{0,i}$ look like in different coordinate spaces, illustrating that the $\dot{x}$–$\dot{y}$ coordinate plane can be used to effectively parametrize the intersection between the quasi-periodic torus and the surface of section $S(\boldsymbol{x})=z$, $\dot{z}<0$. Then, let $R=\sqrt{\dot{x}^2+\dot{y}^2}$, and consider a truncated Fourier series up to the $N_{max}=20$ order such that

$$\boldsymbol{X}_0=\begin{bmatrix}\boldsymbol{x}_{0,1}\\ \vdots \\ \boldsymbol{x}_{0,N}\end{bmatrix}=A(\theta)\boldsymbol{Q}, \tag{33}$$

where $\boldsymbol{Q}=[\boldsymbol{Q}_x^T\ \boldsymbol{Q}_y^T\ \boldsymbol{Q}_R^T\ \boldsymbol{Q}_z^T]^T$ is the $(8N_{\max}+4)\times 1$ Fourier coefficient vector (since $z=0$ on the surface of section, there is no need to compute the corresponding Fourier coefficient vector) and $A(\theta)$ is the $6N\times(8N_{\max}+4)$ matrix defined by

$$A(\theta)=\begin{bmatrix}A(\theta_1)\\ \vdots \\ A(\theta_N)\end{bmatrix},\quad A(\theta_i)=\begin{bmatrix}\mathrm{cs}(\theta_i) & 0 & 0 & 0\\ 0 & \mathrm{cs}(\theta_i) & 0 & 0\\ 0 & 0 & 0 & 0\\ 0 & 0 & \cos(\theta_i)\,\mathrm{cs}(\theta_i) & 0\\ 0 & 0 & \sin(\theta_i)\,\mathrm{cs}(\theta_i) & 0\\ 0 & 0 & 0 & \mathrm{cs}(\theta_i)\end{bmatrix} \tag{34}$$

with

$$\mathrm{cs}(\theta_i)=\big[1\quad \cos(\theta_i)\quad \sin(\theta_i)\quad \cos(2\,\theta_i)\quad \sin(2\,\theta_i)\ldots\cos(N_{\max}\,\theta_i)\,\sin(N_{\max}\,\theta_i)\big]. \tag{35}$$

Now propagate each of the N points till the next surface of section crossing using the full nonlinear equations of motion (14), and compute the corresponding angle in terms of the chosen coordinate variable, i.e.,

$$\theta_{T,i}=\arctan\left(\frac{\dot{y}_i}{\dot{x}_i}\right). \tag{36}$$

If the $\boldsymbol{X}_0$ points were initialized exactly on the invariant set of the Poincaré section, the points obtained after one orbital period, namely $\boldsymbol{X}_T$, would satisfy

$$F(\boldsymbol{Q})=\boldsymbol{X}_T-A(\theta_T)\boldsymbol{Q}=\boldsymbol{0}. \tag{37}$$

Since this is not the case–at least for the very first initial guess–consider updating the Fourier coefficients using Newton's iteration scheme

$$\boldsymbol{Q}^{k+1}=\boldsymbol{Q}^k-DF(\boldsymbol{Q}^k)^{\dagger}\,F(\boldsymbol{Q}^k), \tag{38}$$

where $DF^{\dagger}$ denotes the pseudoinverse of the jacobian matrix of $F(\boldsymbol{Q})$ (see Kolemen's original paper for details on how to compute the Jacobian matrix).

Before that, observe that the researched quasi-periodic invariant tori lie in two-parameter families [20]. Therefore, two additional equations need to be appended to the error vector (37) in order to select a single quasi-periodic invariant torus within its family. It turns out that the best choice of constraints to be added in order to achieve bounded relative motion is made by the projected area of the invariant set in the $\dot{x}$–$\dot{y}$ plane, namely

$$\mathcal{A}=\frac{\pi}{2}\boldsymbol{Q}_R^T\boldsymbol{Q}_R, \tag{39}$$

and the period of the quasi-periodic orbit, i.e.,

$$T=\frac{1}{N}\sum_{i=1}^{N}\tau(\boldsymbol{x}_i), \tag{40}$$

where $\tau(\boldsymbol{x}_i)$ is the time between two consecutive surface of section crossings for the i th trajectory. Accordingly, the final error vector $F(\boldsymbol{Q})$ will be given by

$$F(\boldsymbol{Q})=[\boldsymbol{X}_T-A(\theta_T)\boldsymbol{Q};\ \Delta\mathcal{A};\ \Delta T], \tag{41}$$

where $\Delta\mathcal{A}=\mathcal{A}-\mathcal{A}_{\text{desired}}$ and $\Delta T=T-T_{\text{desired}}$ are the differences between the current and desired values. With these choice of equations, Newton's algorithm (38) usually converges to the desired quasi-periodic torus in four or five iterations.

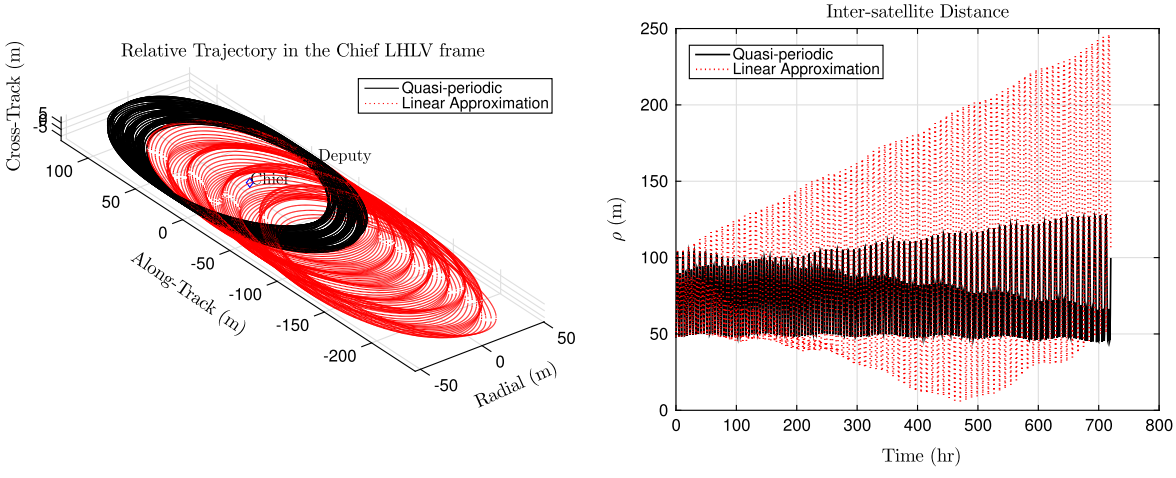

Fig. 11. In-plane Relative Trajectories over 30 days. The chief spacecraft has been initialized on the periodic orbit.

7. Formation flying

By choosing $\lambda = \lambda_{12}$, $\kappa = 50$ m, $\mathcal{A}_{\text{desired}}$ equal to the $\dot{x}$–$\dot{y}$ area of Fig. 10, and T_{desired} equal to the period of the periodic orbit of Fig. 7(b), Kolemen's algorithm converges after four iterations to a quasi-periodic torus that yields the relative motion of Fig. 11. In the plots of Fig. 11, the chief spacecraft has been initialized on the periodic orbit, whereas the deputy spacecraft has been initialized on the surface of the quasi-periodic torus obtained with the Newton iteration scheme. The resulting *in-plane* relative orbit is shown with respect to the LHLV frame of the chief after integrating the equations of motion (14) of both satellites for 30 days.

Although there is some residual drift in the along-track direction, the relative trajectory does not diverge as fast as the relative trajectory computed from the linear approximation of the invariant torus (i.e., using as initial conditions one of the $\boldsymbol{x}_{0,i}$ points created on the invariant set of the monodromy map M). Similar results are also obtained when initializing the deputy spacecraft on the surface of a quasi-periodic torus of the second family, i.e., for $\lambda = \lambda_{34}$, $\boldsymbol{v} = \boldsymbol{v}_{34} = \boldsymbol{v}_3 + \mathrm{i}\,\boldsymbol{v}_4$. The obtained *out-of-plane* relative trajectory is illustrated in Fig. 12.

Another interesting design option would be to initialize both the chief and the deputy satellites on the computed invariant tori. Figs. 13 and 14 display how the relative trajectories look like for spacecraft formations on the first and second center submanifolds respectively. As it can be seen, bounded relative motion about slowly rotating triaxial ellipsoids can be achieved over long time spans; i.e., more than 30 days.

It is important to note that these results are obtained using the full constant density ellipsoidal gravity model of the central body, thus including gravity coefficients beyond the second-order second-degree used for the preliminary analyses at the beginning of this paper. Nevertheless, the plots of Figs. 11–14 also assume perfect initial conditions and do not take into account the effects of other forces such as solar radiation pressure and third body attraction.

As one can expect, the inclusion of these perturbations in the simulations tends to destroy the formations, and active control strategies should be implemented to counter the relative drift induced by external forces and uncertainties in the system. Yet, even in a worst case scenario where the deputy and chief spacecraft are deployed when Toutatis is at perihelion, control would not be necessary for more than 2.5 days (Fig. 15). In this time frame, many scientific operations could still be performed and used to infer valuable information on the mechanical and chemical properties of the target asteroid.

8. Conclusions and future work

By combining analytical and numerical methods, it is possible to come up with a systematic procedure to initialize spacecraft formations about 4179 Toutatis. The problem was first analyzed with a second-order second-degree gravity field, which was initially used to derive first-order differential relationships between the mean orbit elements of the spacecraft. The second-order second-degree bounded relative motion conditions derived in this paper were seeking to minimize the relative drift between the satellite in the formations caused by the elongated shape of the central body. However, this method fails to provide long-term bounded relative orbits because of the approximations and errors in the Lie–Deprit transformation used to carry on the necessary mean-to-osculating orbit element conversions.

Such mapping, however, provides a reliable initial guess for the numerical computation of periodic orbits in the body-fixed frame of the target asteroid (Fig. 7). Since the monodromy matrix computed along these trajectories has two pairs of complex conjugate eigenvalues, the computed periodic orbits are stable and surrounded bytwo families of quasi-periodic invariant tori. Because of this, Kolemen's surface of section approach was applied in order to compute different quasi-periodic tori about Toutatis and establish bounded relative motion [10]. In particular, by choosing the orbital period as one of the

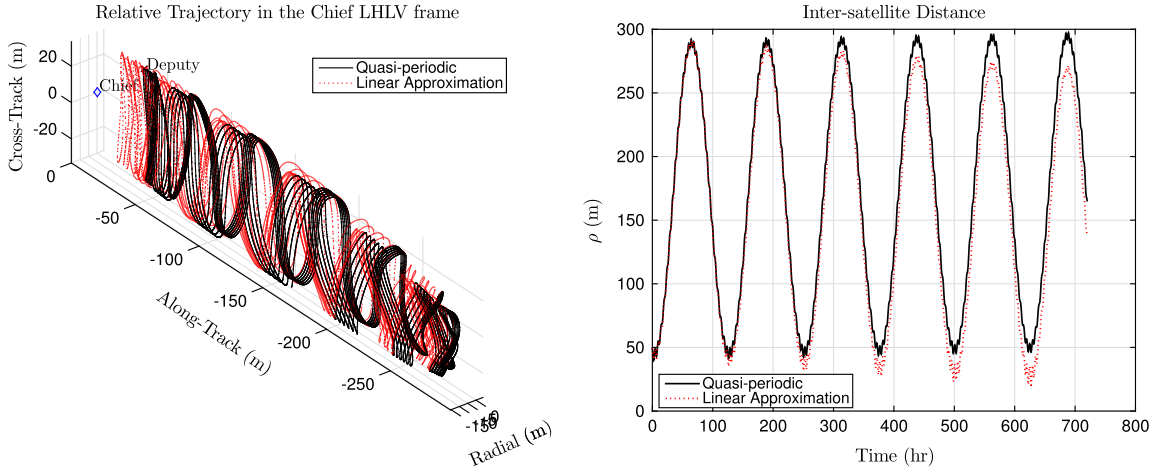

Fig. 12. Out-of-plane Relative Trajectories over 30 days. The chief spacecraft has been initialized on the periodic orbit.

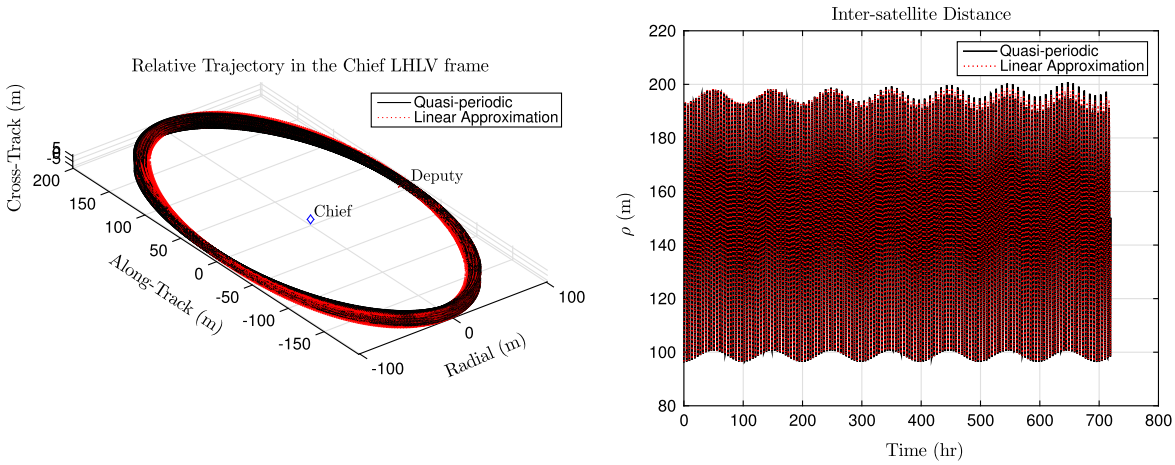

Fig. 13. In-plane Relative Trajectory over 30 days when the satellites are both initialized on the invariant torus.

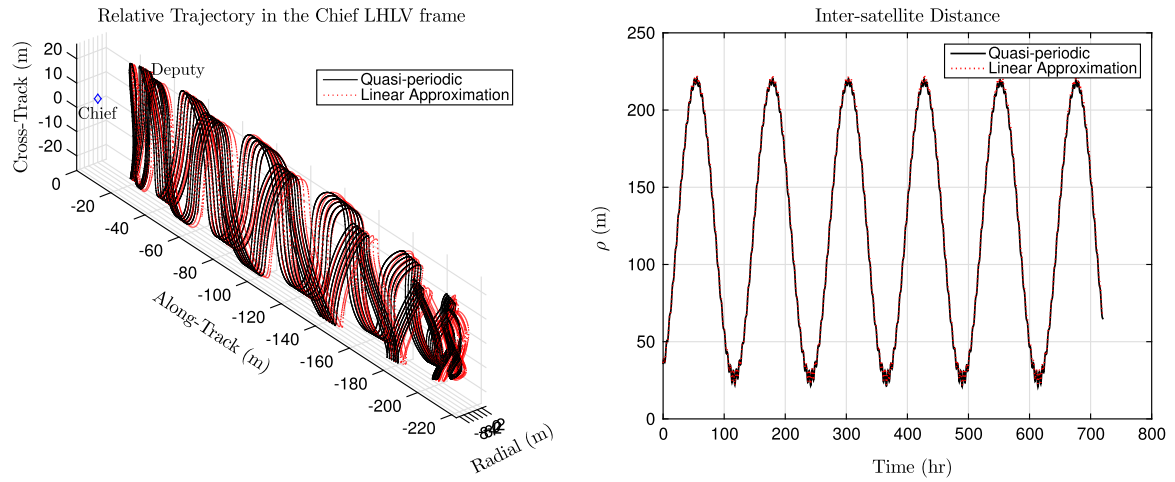

Fig. 14. Out-of-plane Relative Trajectories over 30 days when the satellites are both initialized on the invariant torus.

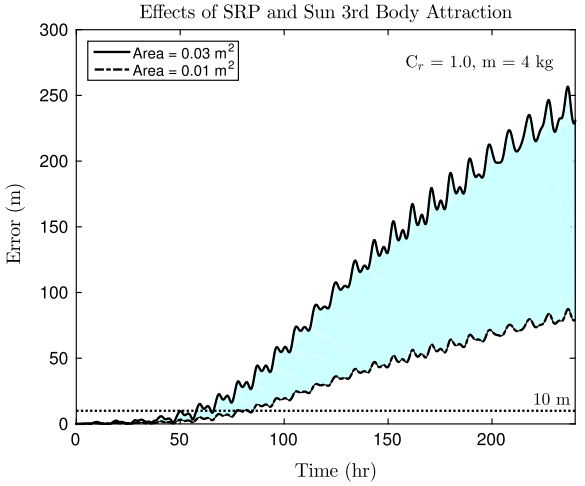

Fig. 15. Effects of SRP and Sun Third body attraction on 3U Cubesat formations about Toutatis at Perihelion. SRP was simulated using the "cannonball" model (see Ref. [21] for details).

parameters in Kolemen's method, it was possible to come up with invariant tori foliated by quasi-periodic orbits that pierce a user-defined surface of section with the same frequency as the underlying periodic orbit. This is an ideal condition for spacecraft formation flying as it yields in-plane and out-of-plane relative trajectories that remain bounded for more than 30 days (Figs. 11–14).

Future work will be focused on extending this approach beyond slowly rotating bodies and applying dynamical systems theory to design spacecraft formations about planets and other small bodies. Furthermore, it will be interesting to investigate the existence of cost-free bounded relative trajectories with more sophisticated gravity fields such as the constant density polyhedron model, which better takes into account the actual physical shape of the target asteroid [22]. Finally, solar radiation pressure should be modeled and included in the equations of motion to improve robustness.

References

[1] C. Maddock, J.P. Sanchez Cuartielles, M. Vasile, G. Radice, Comparison of single and multi-spacecraft configurations for nea deflection by solar sublimation, in: New Trends in Astrodynamics and Applications III, AIP Conference Proceedings, vol. 886, pp. 303–316, 2007.

[2] S. Gong, J. Li, H. BaoYin, Formation flying solar-sail gravity tractors in displaced orbit for towing near-earth asteroids, Celest. Mech. Dyn. Astron. 105 (1–3) (2009) 159–177.

[3] M. Vasile, C.A. Maddock, On the deflection of asteroids with mirrors, Celest. Mech. Dyn. Astron. 107 (1–2) (2010) 265–284.

[4] C. Foster, J. Bellerose, D. Mauro, B. Jaroux, Mission concepts and operations for asteroid mitigation involving multiple gravity tractors, Acta Astronaut. 90 (1) (2013) 112–118.

[5] J. Huang, J. Ji, P. Ye, X. Wang, J. Yan, L. Meng, S. Wang, C. Li, Y. Li, D. Qiao, et al., The ginger-shaped asteroid 4179 toutatis: new observations from a successful flyby of chang'e-2, Sci. Rep. 3 (2013).

[6] W. Hu, D.J. Scheeres, Spacecraft motion about slowly rotating asteroids, J. Guid. Control Dyn. 25 (4) (2002) 765–775.

[7] H. Schaub, J.L. Junkins, Analytical Mechanics of Space Systems. AIAA Education Series, 2nd ed., 2009.

[8] H. Schaub, K.T. Alfriend, J2-invariant relative orbits for spacecraft formations, Celest. Mech. Dyn. Astron. 79 (2) (2001) 77–95.

[9] D.J. Scheeres, Orbital Motion in Strongly Perturbed Environments, Springer, Springer-Verlag, Berlin, Heidelberg, 2012.

[10] E. Kolemen, N.J. Kasdin, P. Gurfil, Multiple Poincaré sections method for finding the quasiperiodic orbits of the restricted three body problem, Celest. Mech. Dyn. Astron. 112 (1) (2012) 47–74.

[11] A. Deprit, Canonical transformations depending on a small parameter, Celest. Mech. 1 (1) (1969) 12–30.

[12] B. De Saedeleer, J. Henrard, The combined effect of j2 and c22 on the critical inclination of a lunar orbiter, Adv. Space Res. 37 (1) (2006) 80–87.

[13] K.C. Howell, Three-dimensional, periodic,'halo' orbits, Celest. Mech. 32 (1) (1984) 53–71.

[14] B. Barden, K. Howell, Formation flying in the vicinity of libration point orbits, Adv. Astronaut. Sci. 99 (1998) 969–988.

[15] R.S. Hudson, S.J. Ostro, Shape and non-principal axis spin state of asteroid 4179 toutatis, Science (1995) 84.

[16] D.J. Scheeres, Dynamics about uniformly rotating triaxial ellipsoids: applications to asteroids, Icarus 110 (2) (1994) 225–238.

[17] W.H. Press, Numerical Recipes 3rd Edition: The Art of Scientific Computing, Cambridge University Press, Cambridge, United Kingdom, 2007.

[18] S.B. Broschart, G. Lantoine, D.J. Grebow, Quasi-terminator orbits near primitive bodies, Celest. Mech. Dyn. Astron. 120 (2) (2014) 195–215.

[19] M. Duering, M. Vasile, M. Landgraf, Uncontrolled spacecraft formations on two-dimensional invariant tori, in: 23rd International Symposium on Spaceflight Dynamics, 2012.

[20] Z.P. Olikara, K.C. Howell, Computation of quasi-periodic invariant tori in the restricted three-body problem, in: 20th AAS/AIAA Space Flight Mechanics Meeting, 2010.

[21] D.A. Vallado, Fundamentals of Astrodynamics and Applications, 3rd ed. Springer, New York, NY, 2001.

[22] R.A. Werner, D.J. Scheeres, Exterior gravitation of a polyhedron derived and compared with harmonic and mascon gravitation representations of asteroid 4769 castalia, Celest. Mech. Dyn. Astron. 65 (3) (1996) 313–344.